

## Convective Precipitation Variability as a Tool for General Circulation Model Analysis

CHARLOTTE A. DEMOTT, DAVID A. RANDALL, AND MARAT KHAIROUTDINOV

*Department of Atmospheric Science, Colorado State University, Fort Collins, Colorado*

(Manuscript received 13 December 2005, in final form 22 May 2006)

### ABSTRACT

Precipitation variability is analyzed in two versions of the Community Atmospheric Model (CAM), the standard model, CAM, and a “multiscale modeling framework” (MMF), in which the cumulus parameterization has been replaced with a cloud-resolving model. Probability distribution functions (PDFs) of daily mean rainfall in three geographic locations [the Amazon Basin and western Pacific in December–February (DJF) and the North American Great Plains in June–August (JJA)] indicate that the CAM produces too much light–moderate rainfall ( $10 \sim 20 \text{ mm day}^{-1}$ ), and not enough heavy rainfall, compared to observations. The MMF underestimates rain contributions from the lightest rainfall rates but correctly simulates more intense rainfall events. These differences are not always apparent in seasonal mean rainfall totals.

Analysis of 3–6-hourly rainfall and sounding data in the same locations reveals that the CAM produces moderately intense rainfall as soon as the boundary layer energizes. Precipitation is also concurrent with tropospheric relative humidity and lifted parcel buoyancy increases. In contrast, the MMF and observations are characterized by a lag of several hours between boundary layer energy buildup and precipitation, and a gradual increase in the depth of low-level relative humidity maximum prior to rainfall.

The environmental entrainment rate selection in the CAM cumulus parameterization influences CAM precipitation timing and intensity, and may contribute to the midlevel dry bias in that model. The resulting low-intensity rainfall in the CAM leads to rainfall–canopy vegetation interactions that are different from those simulated by the MMF. The authors present evidence suggesting that this interaction may artificially inflate North American Great Plains summertime rainfall totals in the CAM.

### 1. Introduction

Evaluation of general circulation model (GCM) performance traditionally begins with comparisons of maps of simulated and observed seasonal-mean quantities (e.g., zonal wind, top of atmosphere radiation balance, precipitation). This approach is useful for precipitation because dominant precipitation mechanisms of a given region are generally known (e.g., summertime thunderstorm activity in southeastern North America, widespread wintertime frontal precipitation in northwestern North America). If a GCM has trouble producing the observed seasonal mean precipitation in a given area, it may actually have trouble representing the locally dominant precipitation mechanism.

Until recently, an issue less frequently explored in model evaluation is the temporal and/or spatial vari-

ability that is superimposed upon the seasonal mean. Seasonal mean precipitation can be affected by a spectrum of temporal scales, and it is possible for a model to generate a “correct” seasonal mean value without properly capturing the underlying precipitation variability (Chen et al. 1996; Dai et al. 1999).

A growing body of work addresses precipitation variability in the real world and in GCMs. Dai (2001) used global rain gauge data to document spatial and seasonal variations of precipitation frequency and intensity. High-frequency precipitation variability was analyzed for North America (Higgins et al. 1996), the Amazon Basin (Liebmann et al. 1999; Petersen et al. 2002), and the Tropics and Northern Hemisphere (Kharin et al. 2005). Karl and Knight (1998) and Groisman et al. (2005) analyzed long-term trends in precipitation intensity, finding increases in the intensity of heavy rainfall events in North America over the past  $\sim 100$  yr. The abilities of GCMs to successfully reproduce observed frequency and intensity variability are only now being documented (Trenberth et al. 2003; Dai and Trenberth 2004; Iorio et al. 2004). Sun et al. (2006) studied seven

---

*Corresponding author address:* Charlotte A. DeMott, Department of Atmospheric Science, Colorado State University, Fort Collins, CO 80523.  
E-mail: demott@atmos.colostate.edu

fully coupled climate models and found that most of them overestimated the frequency of light precipitation and underestimated the frequency of heavy precipitation. Wilcox and Donner (2007) found similar results for the National Oceanic and Atmospheric Administration/Geophysical Fluid Dynamics Laboratory (NOAA/GFDL) Atmospheric Model version 2 (AM2) GCM, noting that simulated precipitation intensity is affected by several aspects of the convective parameterization including the closure, assumed convective triggers, and the spectrum of convective and mesoscale clouds.

Improving our understanding of precipitation characteristics via analysis of GCMs is perhaps best approached by studying high-frequency rainfall variability. A statistically significant sample of high-frequency variability can be obtained in a relatively short simulation or a relatively short observational record. In this paper, we focus on the high-frequency interactions of summertime convection with its environment. We analyze two versions of the Community Atmospheric Model (CAM). The first is the standard configuration, and the second is a “superparameterized” version (described in the next section). Our goals are 1) to gain insight into the interactions between precipitation and the large-scale environment on daily and subdiurnal time scales and 2) to assess the abilities of the two model configurations to simulate the observed range of daily mean rainfall rates and rainfall production mechanisms in a variety of locations. Our goal is not simply to identify needed improvements in either model. Rather, by comparing the successes and/or shortcomings of each model version, we hope to improve our general understanding of how convection responds to and affects larger-scale circulations.

The paper is organized as follows: Model descriptions are given in section 2, and the observational data is described in section 3. Results are presented in section 4, and a discussion is given in section 5. A summary is provided in section 6.

## 2. Model descriptions

We use two versions of the Community Atmospheric Model version 3 (Collins et al. 2004) for this work. The first we refer to simply as the CAM, or CAM3. In stand-alone mode, the CAM is integrated together with the Community Land Model (CLM; Bonan et al. 2002; Oleson et al. 2004) and a “data” ocean in which prescribed sea surface temperatures (SSTs), based on the Reynolds et al. (2002) dataset, are fed via a flux coupler to the overlying atmosphere. The atmosphere does not influence the ocean. The CAM is based on a semi-Lagrangian dynamical core with scalable horizontal

resolution and 26 vertical levels; T42 resolution ( $\sim 2.8^\circ \times 2.8^\circ$ ) was used in the two model runs analyzed here. Each model was run for 500 days with a 1 September start date using climatological SSTs.

Convection is represented in the CAM using the method of Zhang and McFarlane (1995, hereafter ZM95). This approach is based on the detraining plume ensemble concepts of Arakawa and Schubert (1974). Closure is based on the assumption that convection consumes any large-scale convective available potential energy (CAPE), returning the atmosphere toward a neutrally buoyant state over a 1-h convective adjustment time scale. Furthermore, ZM95 assigns a fixed cloud-base mass flux to each plume and includes convective-scale downdrafts, originating from the detraining layer. The implementation of this parameterization into the CAM is described in Zhang et al. (1998). The treatment of shallow convection in the CAM is described by Hack et al. (1993).

The other model configuration we examine is the “multiscale modeling framework” (MMF), which is simply the CAM with a 2D cloud-resolving model running in place of the ZM95 parameterization (e.g., Grabowski 2001). The cloud-resolving model used is the System for Atmospheric Modeling (SAM) of Khairoutdinov and Randall (2003), and its implementation into the CAM is described in Khairoutdinov and Randall (2001) and Khairoutdinov et al. (2005). Although computationally more expensive than the traditional approach, SAM allows for more direct parameterizations of radiation, microphysics, surface energy budgets, and other subgrid-scale processes. As currently configured, SAM is run separately for each GCM grid box, and the simulated convective tendencies are allowed to interact with the large-scale conditions. Each SAM domain is 256 km wide, with 64 columns spaced 4 km apart in the  $x$  direction and 24 vertical levels collocated with the 24 lowest levels of the CAM. The domain is large enough to capture a representative sample of convection within each grid box, with fine enough horizontal and vertical resolution to simulate convective-scale dynamics. Surface topography is currently not included in the SAM. A five-species bulk microphysical parameterization is included in SAM, and radiation calculations are done on the SAM grid, while the surface exchange parameterization is performed on the GCM grid. Detailed comparisons between the CAM and MMF are given in Khairoutdinov et al. (2005). The main differences between the CAM and MMF are 1) the MMF exhibits an improved diurnal cycle of nondrizzle precipitation over land, 2) the MMF produces a more realistic distribution of cirrus cloudi-

ness, and 3) the MMF produces a high precipitation bias in the western Pacific during boreal summer.

### 3. Observational datasets

Precipitation variability is initially analyzed via daily means of simulated and observed precipitation. Our source for daily mean precipitation data is the 1-degree daily (1DD) Global Precipitation Climatology Project (GPCP version 2; Huffman et al. 2001) combined satellite–gauge product. Because precipitation intensity is resolution dependent, the 1DD data is regridded to model resolution before comparisons are made.

Our selection of geographic regions for study was guided by the availability of observational data for model comparison. Our desire to study the high-frequency relationship of precipitation to the environment led us to select locations where surface-based radar data and 3- or 6-hourly sounding data were collected. Intensive observing periods (IOPs) of several major field projects meet this requirement. A description of the three IOPs selected follows, with details of the data processing provided in section 4.

The first region studied is the Amazon Basin. During the winter of 1998/99, the Tropical Rainfall Measuring Mission (TRMM) conducted the Large-Scale Biosphere–Atmosphere (LBA) field campaign (Silva Dias et al. 2002) in southwestern Brazil. Rainfall data from the TRMM 3G68 combined microwave–radar algorithm (Haddad et al. 1997) were used to construct the December–February (DJF) precipitation mean diurnal cycle.

The Atmospheric Radiation Measurement (ARM) program collects data at several locations worldwide. Here, we focus on the Southern Great Plains (SGP) site, which spans northern Oklahoma and southern Kansas. We utilize data from the July 1997 IOP, which was characterized by frequent convective events. Precipitation data is derived from the NEXRAD radar network (Leone et al. 1989; Brown and Lewis 2005) gridded to 4 km  $\times$  4 km resolution over the SGP domain.

The tropical western Pacific is the third area studied, providing an oceanic contrast to the two land-based locations. We use data collected during the Tropical Ocean Global Atmosphere (TOGA) Couple Ocean–Atmosphere Response Experiment (COARE) IOP, conducted from November 1992 through February 1993 (Webster and Lukas 1992). Rainfall measurements were collected from ground- and ship-based disdrometers and two shipboard 5-cm radars. Rainfall estimates were also calculated using sounding data and moisture budget constraints (Johnson and Ciesielski 2000).

The three regions selected for study present chal-

lenges for both the CAM and the MMF, as demonstrated in Fig. 1. In the Amazon Basin, both model versions produce reasonable mean rainfall totals. At the SGP site, the CAM properly simulates observed precipitation amounts, but the MMF grossly underestimates summertime precipitation. In the TOGA COARE region, both simulations overestimate rainfall.

### 4. Results

#### a. Rain-rate PDFs

Daily mean rainfall probability distribution functions (PDFs) of the three regions highlighted in Fig. 1 provide an overview of the range of precipitation rates observed in each region and each simulation. We begin with the TRMM LBA site. PDFs are constructed by binning each DJF daily mean rainfall amount for each grid point into 1 mm day<sup>-1</sup> bins. Results for grid points in the box centered over the TRMM LBA IOP site (see Fig. 1) are expressed as a percentage and are shown in Fig. 2a. Only rainy grid cells are included. For both simulations and observations, rainfall occurs most frequently at low to moderate rain rates ( $\sim < 20$  mm day<sup>-1</sup>). In this range, the PDFs from the CAM and MMF both deviate slightly from the GPCP curve. Rain rates above  $\sim 20$  mm day<sup>-1</sup> represent about 1% of rainy pixels. The MMF does a good job of simulating these high rain rates, but they are underrepresented in the CAM. Multiplying the raw histogram numbers (not the percentages that are plotted in Fig. 2a) by the mean rainfall rate in each bin yields the total rain amount contributed to the seasonal mean by each rain-rate bin. These curves, shown in Fig. 2b, clarify the differences in rainfall production between the model runs and observations. For instance, the absence of high rain-rate contributions to the seasonal mean in the CAM is apparent, as is the overestimate of the rainfall contribution from intermediate rain rates (10  $\sim$  20 mm day<sup>-1</sup>). On the other hand, the MMF does not generate enough rain at light rain rates ( $\sim < 20$  mm day<sup>-1</sup>) and overestimates the contribution from the heaviest rain rates. Converting the curves in Fig. 2b to cumulative distribution (Fig. 2c) illustrates how each PDF results in the seasonal mean rainfall. Fortuitously, the means for the two simulations (the rightmost part of each curve) are nearly identical, and are very close to the GPCP. However, the PDFs show that each simulation achieved its respective seasonal mean via two different paths, illustrating the pitfalls of evaluating model performance via seasonal means.

A different picture emerges for the North American Great Plains (Fig. 3). Here, the CAM produces a realistic seasonal mean, but the MMF simulates much less

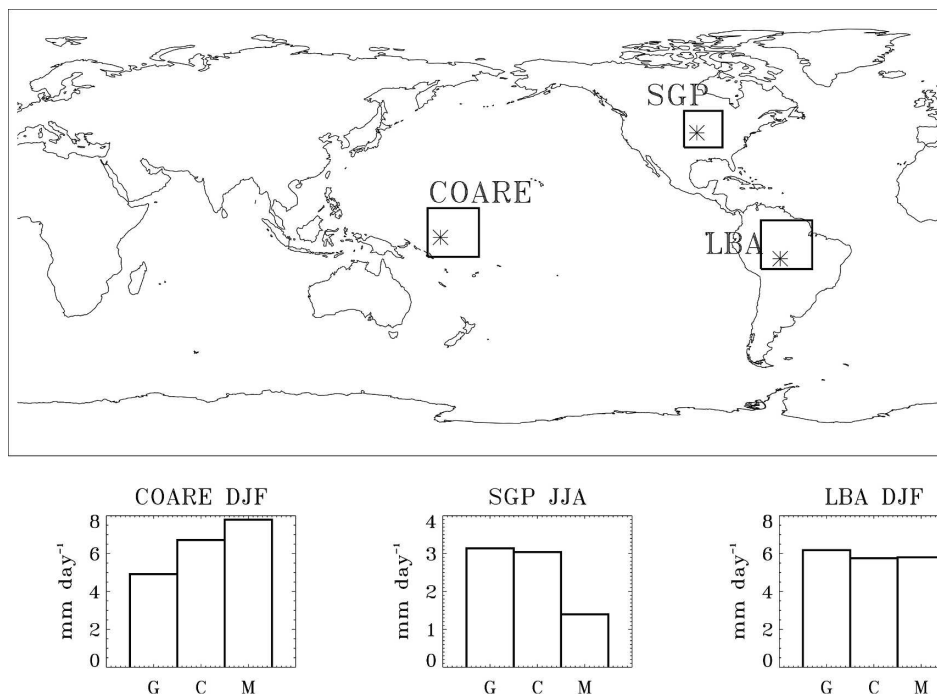


FIG. 1. (top) Locations of rainfall PDF analyses (boxes) and IOP sounding analyses (asterisks). (bottom) Seasonal mean precipitation values for each boxed region for GPCP observations (G), CAM (C), and MMF (M).

rain than is observed (see Fig. 1). The PDFs of daily rain rate (Fig. 3a) for the CAM again show an overabundance of rain rates near  $10 \text{ mm day}^{-1}$  and a deficit of heavy rain rates. Somewhat surprisingly, the MMF produces an appropriate distribution *width*, despite the relative dearth of light and intermediate rainfall rates. Converting the PDFs to rain amount distributions (Fig. 3b) clarifies these differences. The CAM's tendency to

concentrate too much rainfall at  $\sim 10 \text{ mm day}^{-1}$ , already seen in the Amazon Basin, is repeated for the Great Plains, as is the lack of rain at the heaviest rain rates. The MMF's underrepresentation of rain from light to moderate rain rates, also noted for the Amazon Basin, is even more drastic for the Great Plains. The consequence of not producing enough rainfall over a broad range of rainfall rates is seen in the cumulative

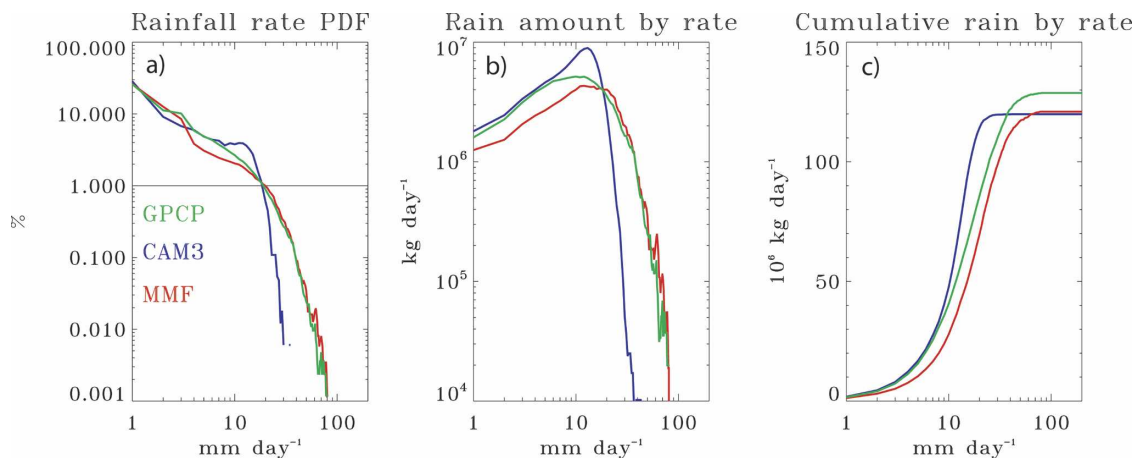


FIG. 2. DJF daily mean rainfall rate distributions for GPCP (green), CAM (blue), and MMF (red) for the Amazon Basin, LBA boxed area in Fig. 1: (a) rainfall rate expressed as a percentage of rainy pixels, (b) contribution to seasonal rainfall total as a function of rainfall rate, and (c) cumulative contribution to seasonal rainfall total as a function of rainfall rate. The maximum value of each curve in (c) is the seasonal mean rainfall total for the boxed area.

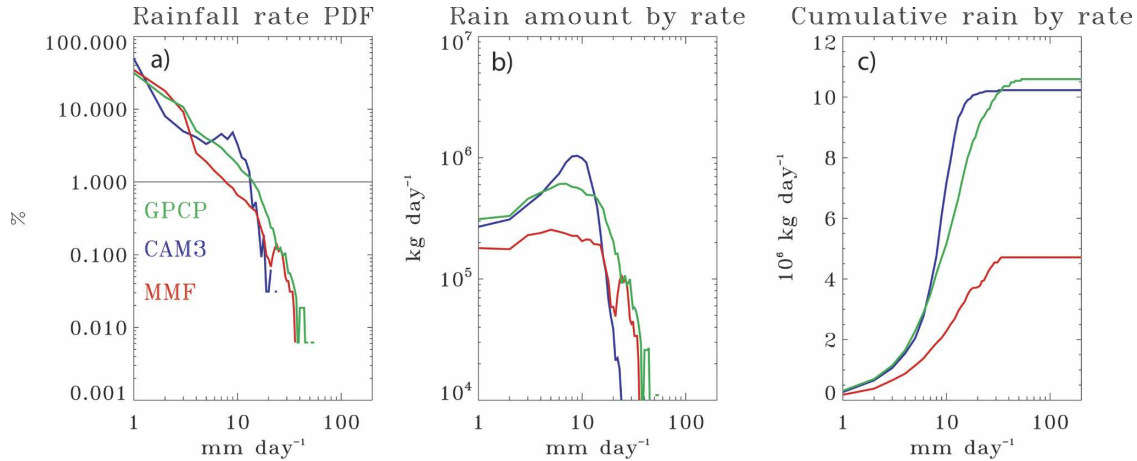


FIG. 3. As in Fig. 2 but during JJA for the North American Great Plains.

distribution curves (Fig. 3c), where the MMF produces less than half of the expected summertime precipitation. Although the CAM again produces a respectable seasonal mean, it does so in a manner not consistent with observations.

The behaviors exhibited by each simulation over land are repeated in the western Pacific (Fig. 4). The daily rain rate PDF in the CAM (Fig. 4a) is too narrow and peaks too sharply at  $\sim 10$  mm day<sup>-1</sup>. The MMF's PDF is too broad, indicating that too much rainfall is produced by overly intense convection. The rain amount curves (Fig. 4b) show that the MMF simply produces too much rainfall at all rain rates, although there is no bias toward any particular rain rate. The 10 mm day<sup>-1</sup> peak in rainfall production in the CAM and the general absence of rainfall production from the heaviest rain rates is also clearly evident. The cumulative rainfall plots (Fig. 4c) reveal that both simulations, especially the MMF, overestimate seasonal mean precipitation.

This initial analysis reveals some persistent biases in rainfall production for each simulation. First, the CAM compensates for heavy rain rate underestimates by overproducing rainfall at intermediate rain rates. The MMF produces more realistic rain rate distribution *widths* but, within this distribution, it underpredicts light rain rates and sometimes compensates by generating too much rainfall at the heaviest rain rates.

The question of whether the MMF underestimates light rain rates as a result of its relatively coarse 4-km resolution, and possible lack of small-scale convection, was examined in a limited run using a 1-km version of the SAM. For the Amazon DJF season, the 1-km run slightly increased the prevalence of the lightest and heaviest rain rates (not shown) but decreased moderate rain rates. Results were similar for the TOGA COARE region. While the finer resolution offered some improvement, it appears that it cannot fully explain the MMF deficiencies. Ultimately, to explain why the CAM

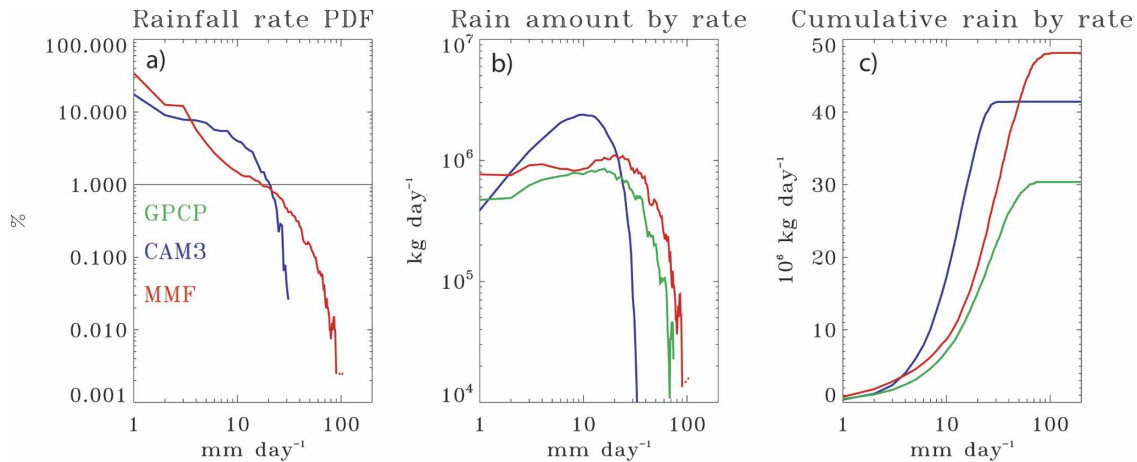


FIG. 4. As in Fig. 2 but for DJF in the western Pacific Ocean.

does not produce higher rain rates, or why the MMF does not generate more rain from light rain rates, we must look beyond daily mean precipitation values.

### *b. Composite diurnal cycles*

Since the diurnal cycle happens every day, it is relatively easy to gather a statistically significant sample of events, both from model output and field data. Its composite can yield insights into the controls of precipitation timing and intensity, especially in cases where the diurnal cycle strongly modulates precipitation.

Here, we examine the mean diurnal cycles of precipitation, CAPE, convective inhibition (CIN), and boundary layer moist static energy ( $h$ ) derived from both model output and observations. The observed diurnal cycle of precipitation is derived from a variety of ground- or space-based sensors, depending on what is available for each location. All other quantities are derived from sounding data. CAPE and CIN are computed using code adapted from that developed by Emanuel (1994). We have chosen the conventional definition of CAPE, which is the vertically integrated positive virtual temperature difference between a pseudoadiabatically lifted parcel and its environment between the level of free convection for a parcel originating from the boundary layer and its level of neutral buoyancy. The CIN is the vertical integral of the virtual temperature difference from the environment for the same parcel below the level of free convection.

#### 1) AMAZON BASIN

During the TRMM LBA balloonborne sondes were launched from four different locations within the study area (Petersen et al. 2002). Launch frequency varied from station to station and a fixed schedule was not strictly maintained during the IOP, although launches occurred at multiples of 3 UTC. Sounding quality control procedures are described in Roy and Halverson (2002). The mean diurnal cycle of sounding-derived variables was computed using the method of Sobel et al. (2004). TRMM rainfall data (product 3G68) were averaged over a  $40 \text{ km} \times 30 \text{ km}$  area centered on the TRMM LBA study area. The ground-based TOGA 5-cm radar provided regular rainfall estimates over a 300-km diameter circle. The diurnal cycle of rainfall computed from the ground-based radar (not shown) compares well with that obtained from the TRMM sensors.

Mean diurnal cycles for model output and observations are shown in Fig. 5. Beginning with the top panels (Figs. 5a–c), both simulations and observations have CAPE (CIN) maximizing (minimizing) in late after-

noon, but the overall amplitude of these two variables is weak in the CAM. Boundary layer moist static energy,  $h$  (Figs. 5d–f), increases sharply at approximately 0800 local time in all three panels, consistent with the onset of morning insolation. The weak amplitude of the diurnal cycle of  $h$  in the CAM is consistent with the weak amplitudes of CAPE and CIN in that model. The convective closure used in the CAM ensures that the CAPE does not vary much during convectively active periods.

The mean diurnal cycles of rainfall (Figs. 5g–i) show that, in both simulations and observations, CAPE, CIN, and  $h$  all begin to increase at 0800 local time. In the CAM, rainfall also increases abruptly at this time and reaches peak intensity at 1400 local time. This behavior in the CAM contrasts with that seen in the MMF and observations, where at 0800 local time rain amounts either increase slowly or decrease somewhat (in the observations) before building to an evening peak.

#### 2) CENTRAL PLAINS

During the July 1997 IOP at the ARM SGP site, 3-hourly soundings were launched from several stations. Data were interpolated to a common vertical resolution using the variational method of Zhang and Lin (1997) and Zhang et al. (2001). Interpolated sounding data and radar-derived rainfall data are available from the ARM Archive Web site (<http://www.archive.arm.gov/>).

Composite diurnal cycles for the SGP are presented in Fig. 6. We again see the late afternoon increase (decrease) of CAPE (CIN) in Figs. 6a–c. In contrast to the Amazon Basin, however, CAM and MMF CAPE have similar amplitudes and are weak compared to the observations. Note that the highest CIN values are seen in the MMF, roughly double that seen in observations and approximately 50% larger than in the CAM. Boundary layer  $h$  (Figs. 6d–f) behaves similarly in the MMF and CAM, although it lacks the strong amplitude seen in the observations, particularly the early morning minimum. Differences are also found in composite diurnal cycles of precipitation (Figs. 6g–i). Compared to the observations, the CAM has an excessively strong diurnal cycle and does not produce enough rainfall during the nighttime hours. The MMF simply does not rain enough. Although CIN is somewhat greater in the MMF than in the CAM, it is not totally prohibitive for convection, as some does occur in the MMF.

#### 3) WESTERN PACIFIC

During TOGA COARE, soundings were launched every 6 h from a set of nested sounding arrays. The

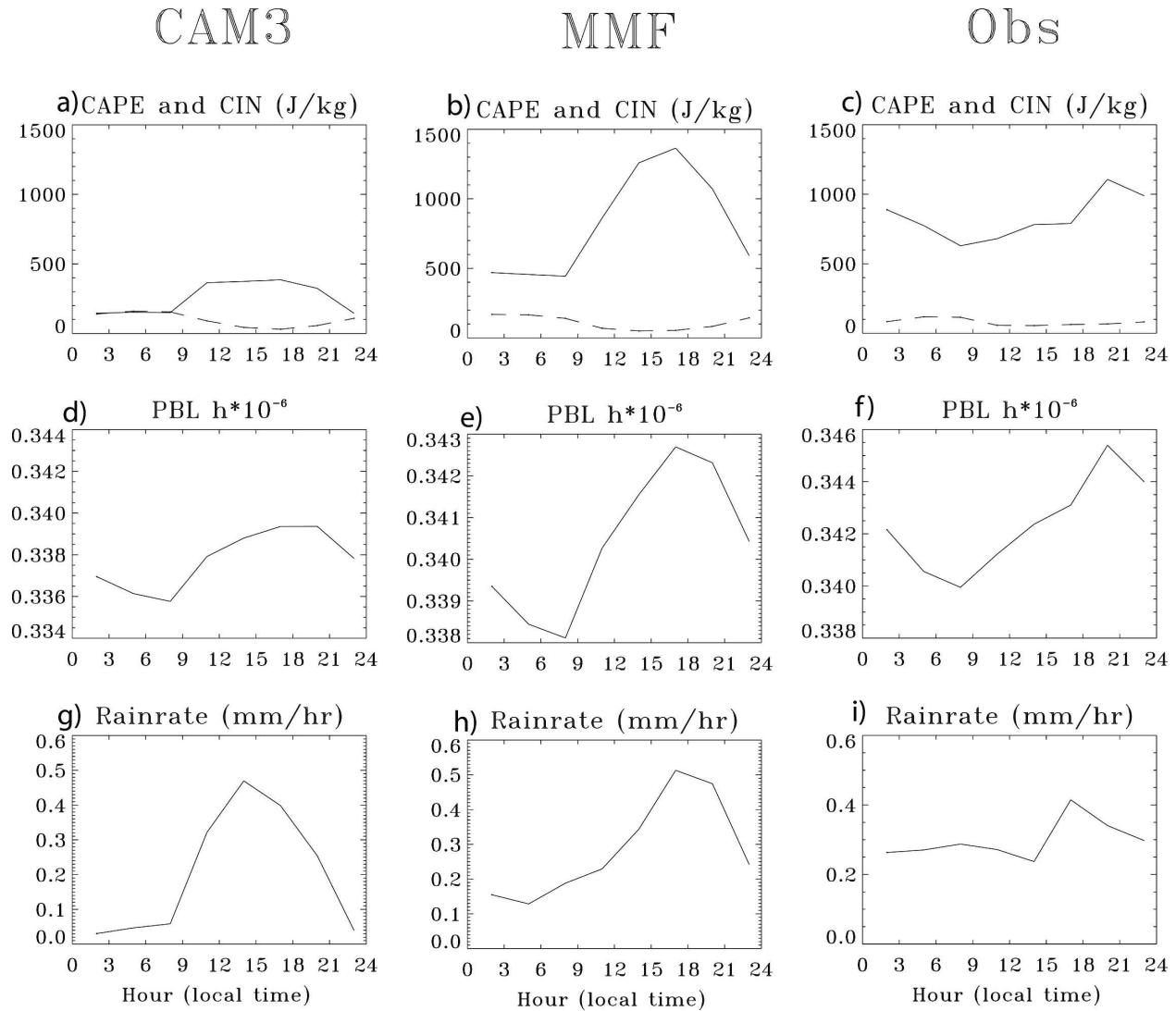


FIG. 5. Composite diurnal cycles for the DJF TRMM at the LBA grid point shown in Fig. 1 for (left) CAM, (middle) MMF, and (right) observations: (a)–(c) CAPE (solid) and CIN (dashed); (d)–(f) boundary layer moist static energy ( $\text{J kg}^{-1}$ ); and (g)–(i) rainfall rate. All times are local.

sounding data has been quality controlled and merged into a single time series by Ciesielski et al. (2003). Radar-based rainfall estimates were used to calibrate sounding-based rainfall retrievals, and the two time series were merged into a continuous product with 6-hourly temporal resolution by Johnson and Ciesielski (2000).

Mean diurnal cycles from the TOGA COARE IOP are shown in Fig. 7. The primary difference between this location and the two continental sites is the expected absence of a strong oceanic diurnal cycle in most of the variables. The CAPE and CIN time series (Figs. 7a–c) show almost no diurnal cycle in the models, and only a weak diurnal cycle in the observations. The

MMF produces realistic diurnal amplitudes of the CAPE and CIN, but those simulated by the CAM are weak. Boundary layer  $h$  (Figs. 7d–f) is similarly too weak in the CAM, and also underestimated in the MMF. The diurnal cycle of precipitation (Figs. 7g–i) is strongest in the MMF and weakest in the CAM. Overall, the diurnal cycle is too weak to be a useful tool for studying the relationships between rainfall and the environment in this region.

Despite the location-to-location differences seen in the mean diurnal cycles, some common themes emerge. The CAM tends to produce weak CAPE and CIN values, but often reasonable rainfall totals. CAM precipitation increases are concurrent with boundary layer  $h$

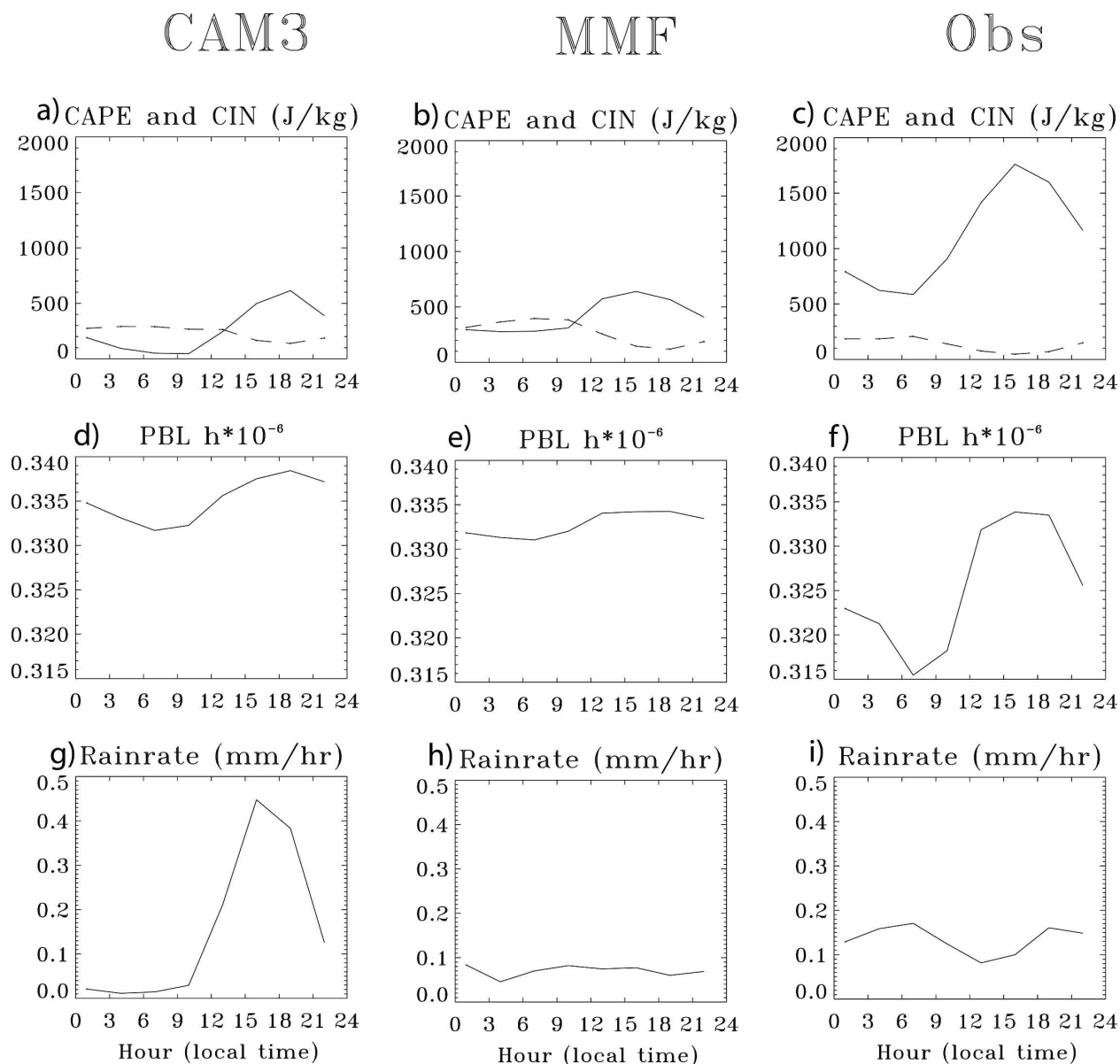


FIG. 6. As in Fig. 5 but for JJA ARM at the grid point labeled SGP in Fig. 1.

increases. Results from the MMF are harder to summarize, due to the drier climate simulated in the SGP and the lack of diurnal cycle in the western Pacific. The most robust result obtained from the MMF mean diurnal cycle analysis is the more realistic timing of rainfall production in the Amazon Basin, relative to the CAM.

### c. Lag-correlation analysis

An alternative approach to studying high-frequency precipitation variability and timing in relation to the state of the atmosphere is lag-correlation analysis. Such an analysis can provide insight into how tightly coupled

precipitation is to other variables, and sharper details of the timing between the two. The data requirements for such a study are daunting, however, because we need continuous, high-quality rainfall and sounding data with a 3–6-hourly temporal resolution.

#### 1) AMAZON BASIN

Rainfall data for this analysis was obtained from the ground-based TOGA radar operated during the TRMM LBA. Data have been averaged into 3-hourly time bins. The four-station network of soundings available during the analysis period were merged as follows:

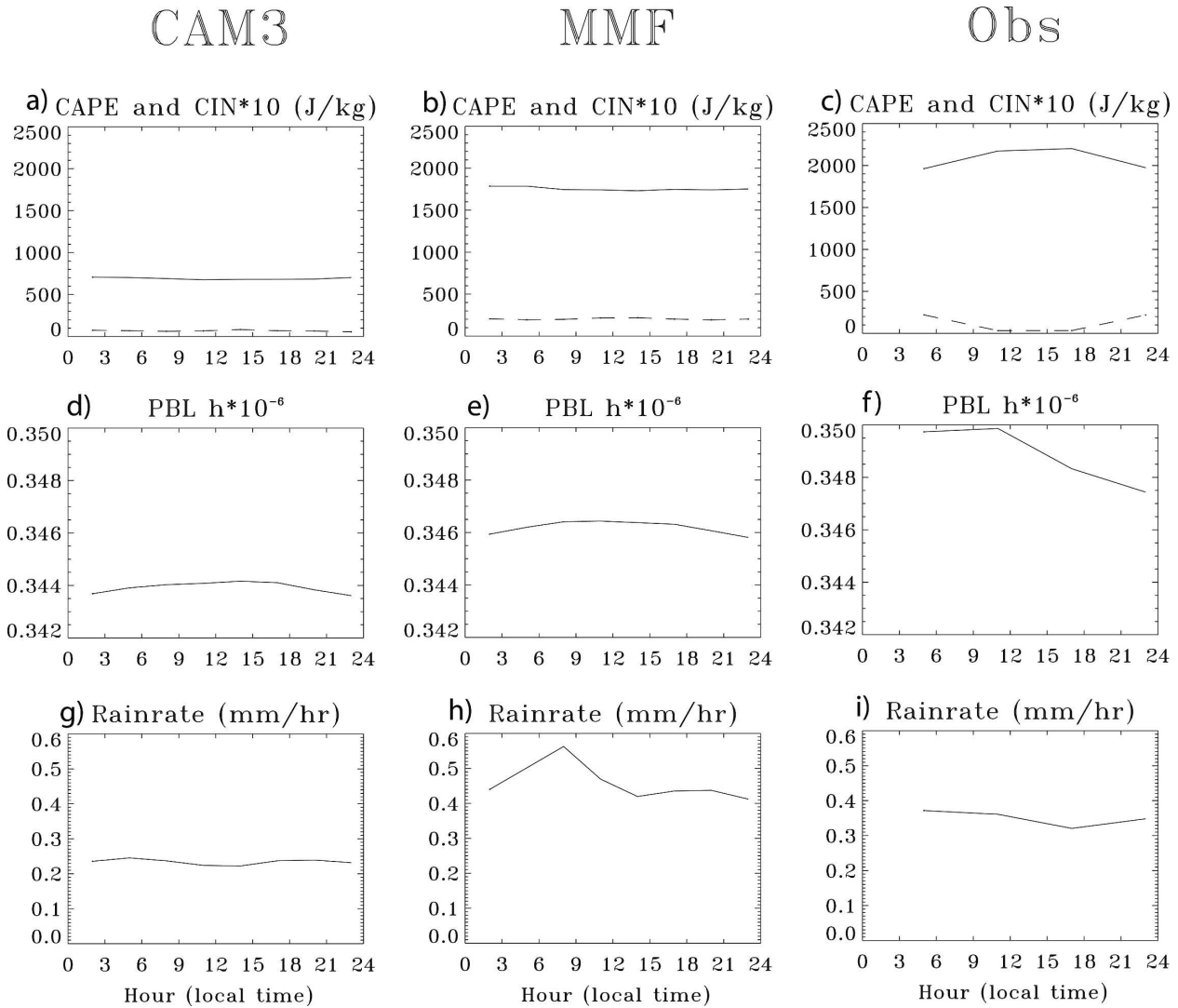


FIG. 7. As in Fig. 5 but for DJF IFA at the grid point labeled COARE in Fig. 1.

mean diurnal cycles of CAPE, CIN, relative humidity, and parcel buoyancy (the virtual temperature difference between a parcel lifted from the boundary layer and its environment) were computed for each sounding. Data calculated from individual soundings were converted to  $z$  scores (normalized standard deviations) based on the mean and standard deviation for that location and time bin, then averaged for each 3-hourly time interval. The resulting time series still contained many gaps. Data gaps of one time step were interpolated, based on the results of autocorrelation analysis of humidity and buoyancy during a 7-day period of continuous sounding data. Analyses based on this interpolated time series are presented in Fig. 8. Rainfall is correlated with boundary layer  $h$ , and relative humidity and buoyancy at all available levels at positive and

negative lags. Negative (positive) lag means that the variable of interest leads (lags) rainfall.

We first examine the relationship of rainfall to boundary layer moist static energy,  $h$  (Figs. 8a–c). In the CAM, rainfall and  $h$  vary coincidentally in time, similar to what was seen in the mean diurnal cycle (Fig. 5a). The two minima in the  $h$ –rainfall lag-correlation plot are separated 24 h, an artifact of the dominant diurnal cycle in the CAM. In the MMF,  $h$  maximizes ahead of rainfall and decreases substantially after a rain event. The two minima in this panel are also separated by 24 h, but the minima at +9 h is much lower than the first. The increase in  $h$  prior to a rain event, and its subsequent decrease following a rain event, are clearly seen in the observations.

The rainfall–relative humidity relationship differs be-

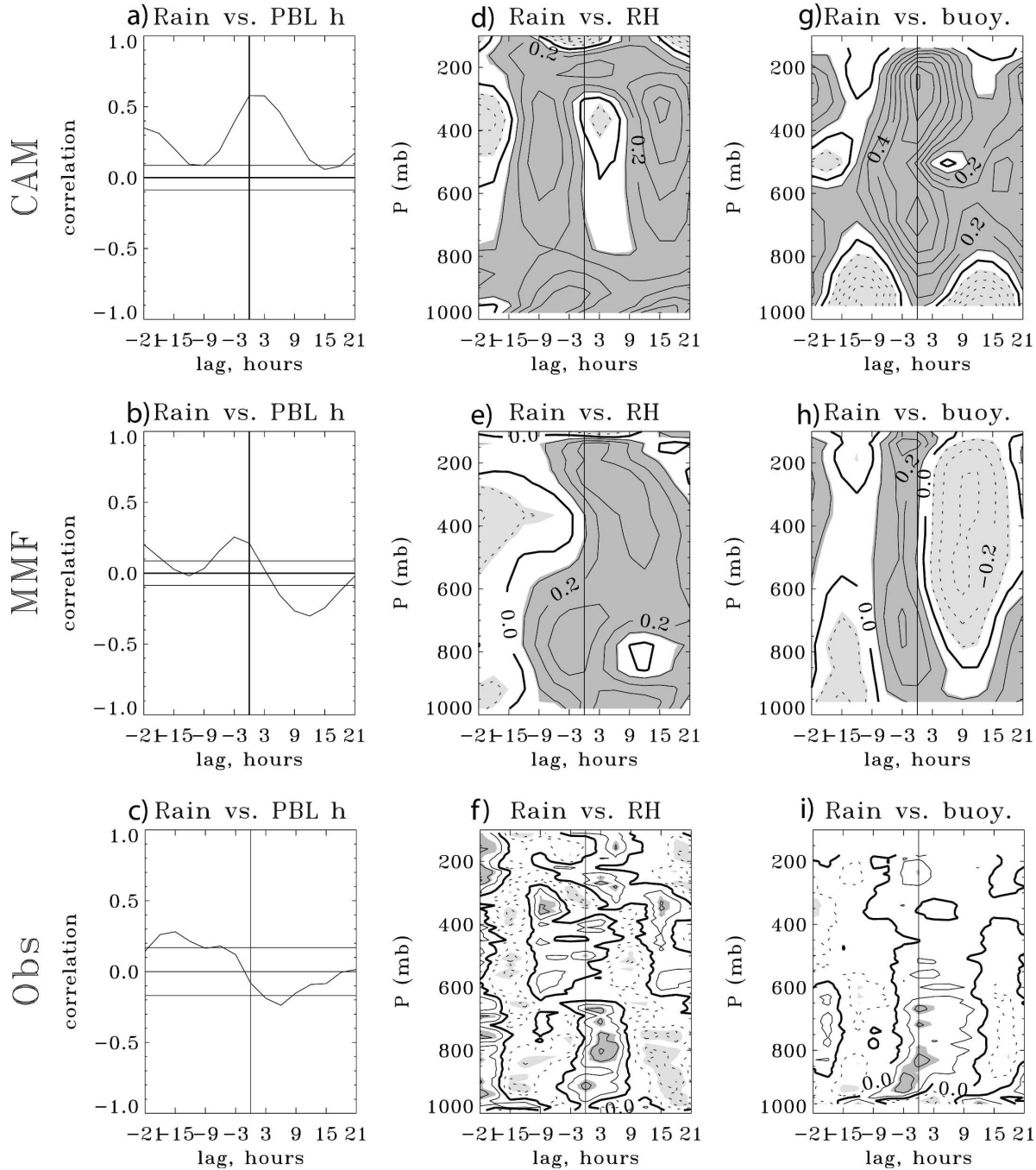


FIG. 8. Correlations between 3-hourly DJF TRMM rainfall and (a)–(c) boundary layer moist static energy, (d)–(f) relative humidity, and (g)–(i) boundary layer parcel buoyancy at various lags for (top row) CAM, (middle row) MMF, and (bottom row) LBA observations. Negative (positive) lag indicates that the plotted variable leads (lags) rainfall. Correlations corresponding to the 95% confidence interval are indicated with horizontal lines in (a)–(c), and dark (light) shading for positive (negative) correlations in (d)–(i). Degrees of freedom are based on the number of independent samples of the rainfall time series.

tween the two simulations (Figs. 8d–f). In the CAM humidity increases over the depth of the troposphere several hours prior to precipitation, with those increases concentrated at low and high levels of the tro-

posphere (i.e., it is vertically decoupled). Humidity decreases at upper levels following a rain event, with another increase seen about 15 h later. When the lag-correlation analysis is extended to  $\pm 45$  h (not shown)

this secondary increase at 15 h is seen to be simply the first in a series of maxima anchored by the diurnal cycle (the two maxima in the plot are exactly 24 h apart). In contrast, several time steps prior to a rain event in the MMF, midlevel moisture gradually increases in magnitude and depth. Following rainfall, the upper and lowest levels moisten. Results from the observational data are disappointing in that the method used to merge the sounding data appears to retain too much intersounding noise to produce a clear signal.

Finally, we examine the relationship of rainfall to the lifted parcel buoyancy profile (Figs. 8g–i). As with the boundary layer  $h$ , we see that rainfall and deep (but vertically decoupled) buoyancy are coincident in the CAM, with the two low-level minima separated by 24 h. In contrast, MMF buoyancy leads precipitation by about three hours and is concentrated at low levels. Correlations based on the sounding data are once again noisy and hard to interpret. It appears that buoyancy at the lowest levels increases about three hours prior to a rain event, but the signal is weak at upper levels.

## 2) GREAT PLAINS

The 3-hourly rainfall and sounding data used to construct the mean diurnal cycle plots required no additional processing for the lag-correlation analysis. Results are presented in Fig. 9. Rainfall and  $h$  (Figs. 9a–c) vary coincidentally in the CAM, with a period of 24 h. In the MMF, there is essentially no signal, owing to the weak rainfall in this region. However, the observations show a gradual buildup of  $h$  several hours prior to a rain event, a decrease as rain falls, and then a minimum following the rain event.

Rainfall–humidity variations (Figs. 9d–f) resemble the results from the Amazon Basin. In the CAM, low- and upper-level relative humidity maxima slightly lead rainfall but are strongly vertically decoupled from one another. Evidence of a 24-h periodicity is clearly evident. Correlations between rain and humidity in the MMF are surprisingly strong, given the overall lack of simulated rainfall, but suggest a low- to midlevel increase in relative humidity prior to a rain event and a vertically and temporally broad increase in column humidity following rainfall. This sequence of events is more distinct in the observations, with clear indications of a deepening layer of low-level humidity preceding a rain event and progressively deeper humidity increases after rainfall.

The relationship of rainfall and parcel buoyancy, shown in Figs. 9g–i, is distinctly different in each of the three panels. CAM rainfall is positively correlated with buoyancy at zero lag throughout the depth of the tro-

posphere, especially at upper levels. MMF rainfall is positively correlated with upper-level buoyancy, most strongly at negative lags (prior to a rain event), but is otherwise difficult to interpret. In the observations, buoyancy builds at low levels before a rain event and decreases after rainfall.

## 3) WESTERN PACIFIC

Analysis for the western Pacific is based upon the 6-hourly data from the TOGA COARE IOP and is presented in Fig. 10. For the rainfall–boundary layer  $h$  relationship (Figs. 10a–c), the diurnal cycle effects are now gone from the CAM, but the zero-lag maximum between the two variables is still present. In the MMF,  $h$  again leads rainfall by several hours, decreases during rain events, and reaches a minimum after rainfall. The observations suggest a similar sequence of events.

Rainfall–humidity covariability is shown in Figs. 10d–f. The CAM produces a better lead–lag progression of the humidity field, but decoupling of the upper- and lower-level humidity is still present. There is no gradual deepening of a moist layer prior to rainfall. The MMF results differ in that humidity increases substantially over an increasingly deep layer prior to the onset of rainfall, with moistening reaching the highest levels after rainfall. The observations are very similar to the MMF results.

Rainfall–buoyancy covariability (Figs. 10g–i) also illustrates the similarities between the MMF and observations, both of which contrast with the CAM results. As in the two continental locations, rainfall in the CAM is most strongly correlated with buoyancy at zero lag. In the MMF and observations, buoyancy increases at low levels prior to a rain event, and then reaches a minimum several hours after rain falls.

The lag-correlation analysis provides information about the nature of rainfall and its environment, and also about the usefulness of our data and model output. In the following discussion, results from two analyses are excluded. First, we do not consider the MMF results from the ARM SGP site because the infrequency of simulated SGP rainfall makes it difficult to say anything meaningful about the convection–environment interaction. Second, we do not consider the sounding-based observations for the Amazon Basin, because the sounding–merging process has obscured any signals that may be present. A compilation of the remaining analyses is summarized in Table 1. When presented in this manner, we see that the high-frequency covariability of rainfall and selected environmental variables in the MMF and observational data are similar to one another, while covariability in the

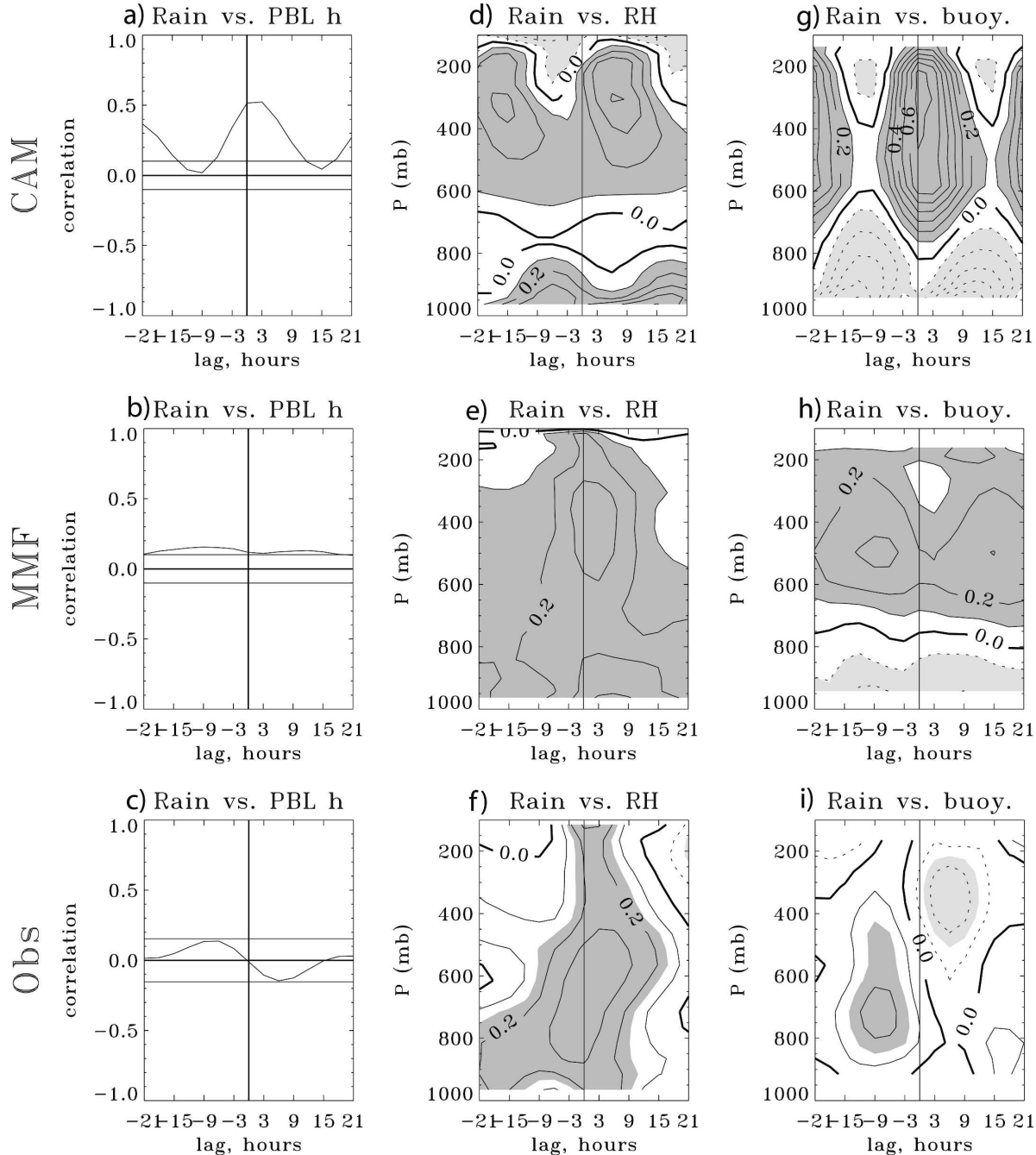


FIG. 9. As in Fig. 8 but for JJA ARM at the SGP grid point.

CAM is different. Physical interpretations of this analysis are given in the next section.

## 5. Discussion

Before suggesting physical interpretations of our results, we give a brief summary of the differences between CAM and MMF precipitation variability. Daily mean rain rate PDFs reveal that the CAM produces too

much rainfall at light to intermediate rain rates. The MMF underestimates rain contributions from the lightest rain rates but correctly produces the heaviest rain rates. In the CAM, there is little or no lag between boundary layer energy buildup and rainfall, whereas the MMF successfully simulates the observed increase (decrease) in boundary layer  $h$  prior to (following) a rain event. The CAM simulates a pervasive decoupling between upper- and lower-level relative humidity

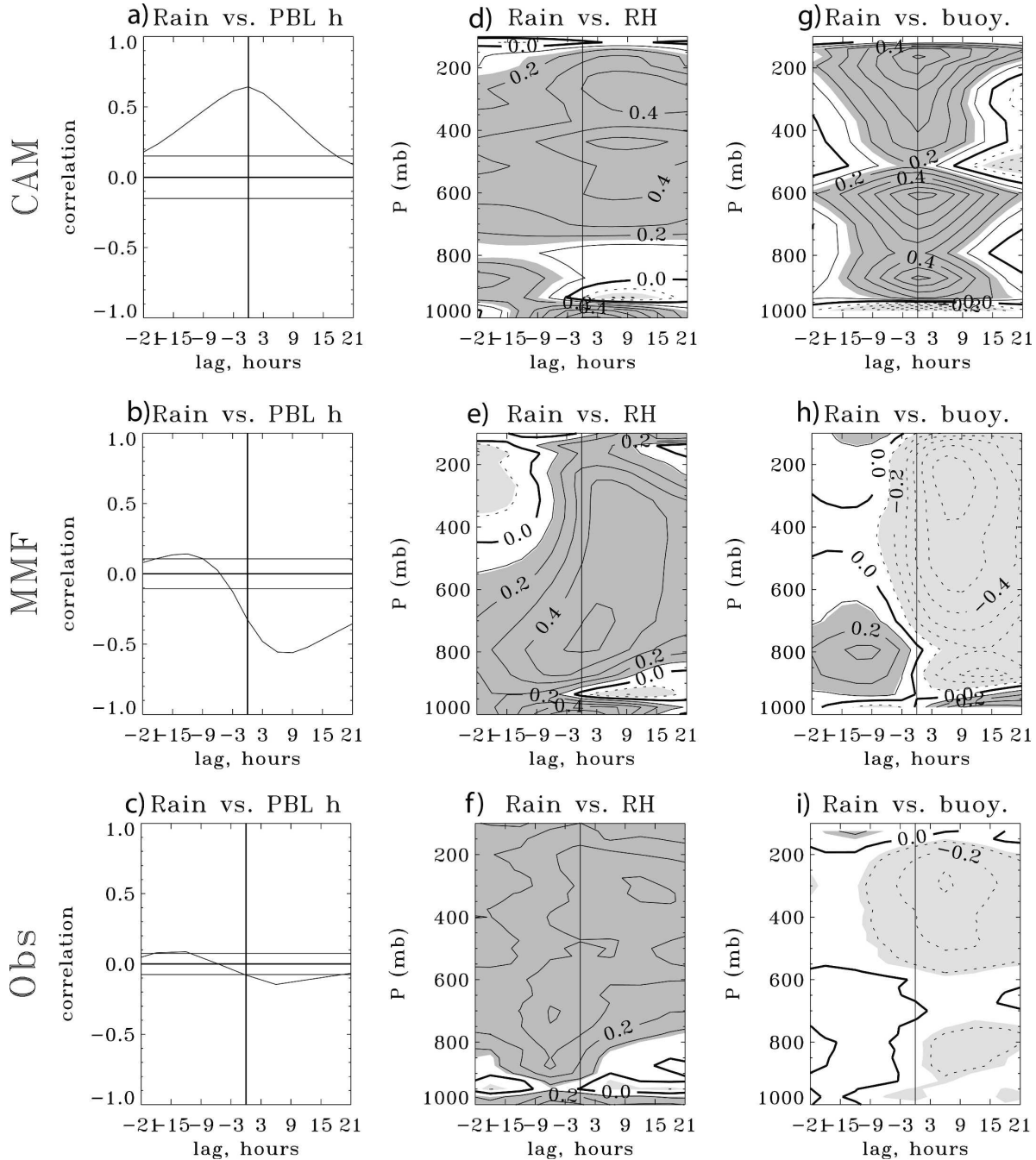


FIG. 10. Same as in Fig. 8 but for DJF IFA at the COARE grid point. Temporal resolution of observational data is every 6 h.

maxima, while no such decoupling is observed, or simulated by the MMF.

Our results can be interpreted physically by asking the simple question: How does it rain? The above analysis suggests the following sequence of events: The boundary layer energizes, producing a positive buoyancy profile, and supports development of initial convective plumes. These initial plumes detrains before at-

taining significant depth and deepen the low-level moist layer, allowing subsequent plumes to attain greater heights before detraining. Each successive “wave” of plumes consumes boundary layer  $h$ . Eventually, the lower troposphere moistens enough to support deep convection and heavy rainfall. The remnants of the deep convective clouds moisten the upper troposphere. This series of events has also been observed in the west-

TABLE 1. Summary of results of lag-correlation analysis for models and observations.

Rain vs:	CAM	MMF	Observations
PBL $h$	Coincident; diurnal cycle over land	Builds prior to rain; minimizes following rain.	Builds prior to rain; minimizes following rain.
Relative humidity profile	Diurnal cycle over land; upper-, lower-level decoupling	Low-level RH increases before rain; upper-level RH increases after rain	Low-level RH increases before rain; upper-level RH increases after rain
Buoyancy profile	Rain nearly coincident with buoyancy	Positive buoyancy anomaly leads, especially at low levels; negative buoyancy anomaly follows rain	Positive buoyancy anomaly leads; negative buoyancy anomaly follows rain

ern Pacific Kwajalein Experiment (KWAJEX) site by Sobel et al. (2004). Our analysis shows that this progression is realistically simulated by the MMF when sufficient low-level moisture is available, but the CAM does not simulate the observed lags.

The following discussion focuses on two general topics. First, why does the CAM lack heavy rainfall, and why is its rainfall so tightly linked to the diurnal cycle? Second, why does the MMF produce so little summertime rainfall over the Great Plains?

#### a. Precipitation timing and intensity in the CAM

We believe that the reason the CAM does not produce the observed sequence of events surrounding a rain event relates to the formulation of its cumulus parameterization, as described in ZM95. In the CAM, convection is permitted when CAPE is present. A spectrum of convective plumes is activated. A key feature of the ZM95 convection parameterization relates to the selection of the environmental entrainment rate associated with the plumes. The ensemble of plumes is limited to updrafts that detrain at or above the height of minimum moist static saturated energy,  $h^*$ . The entrainment rate is adjusted so that this condition is met.

Figure 11 presents time series of relative humidity, rainfall, and the height of minimum  $h^*$ ,  $z_{h^*min}$ , over the SGP grid point for the CAM, MMF, and observations. In the CAM (Fig. 11a), the diurnal covariability between precipitation and low-level relative humidity is readily observed. However, pervasive midlevel dryness is the most salient feature of this time series. The crux of our argument lies with the relationship between the  $z_{h^*min}$  time series and the upper-level relative humidity maxima. Because cumulus detrainment is only allowed

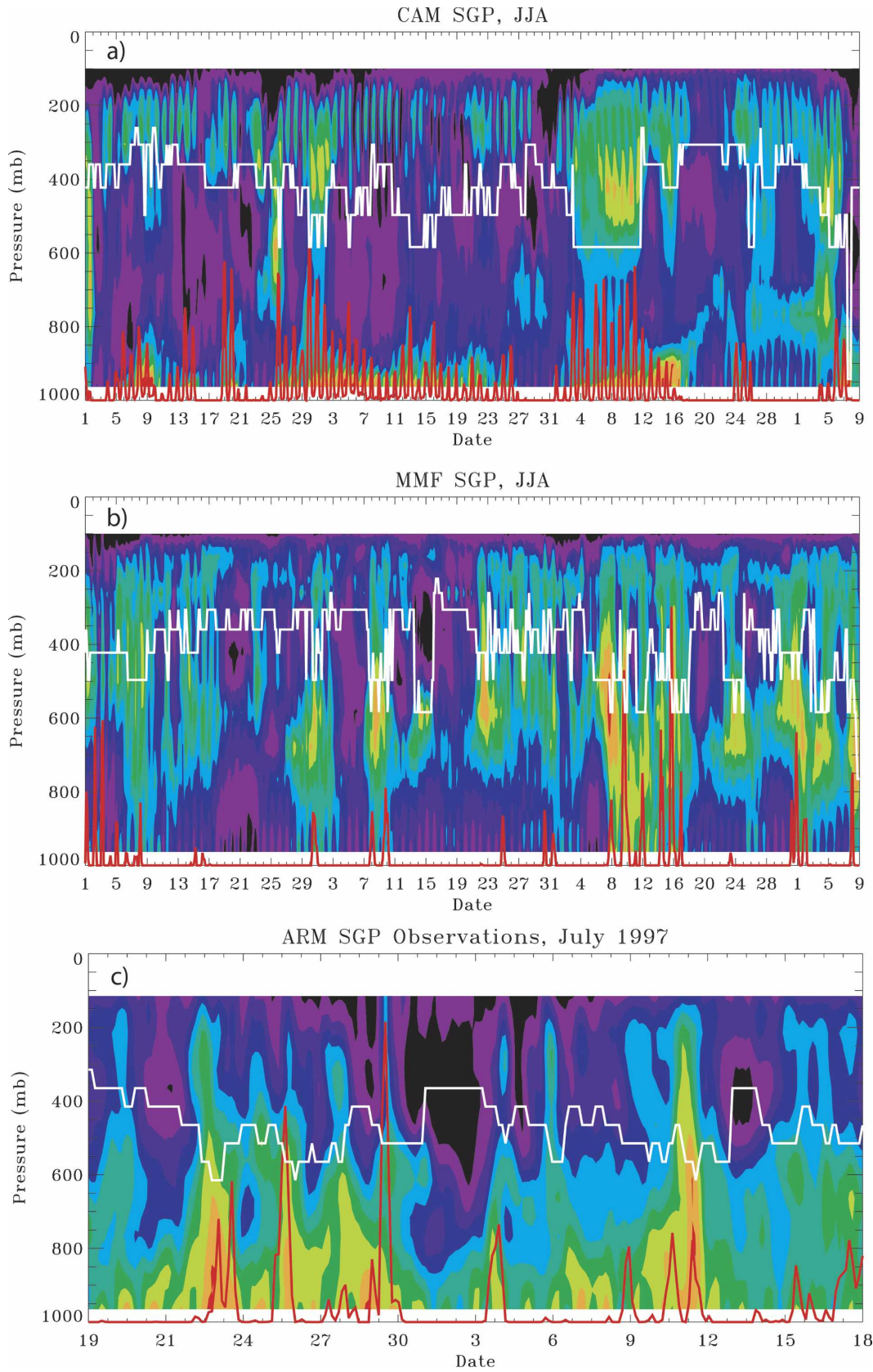
to occur at or above  $z_{h^*min}$ ,  $z_{h^*min}$  appears as a “shelf” upon which higher relative humidity air rests. The shallow convective scheme of Hack et al. (1993) partially offsets this affect (e.g., 25 June and 3 July), but only intermittently (i.e., not with the daily frequency of the ZM95 scheme). Comparison of the MMF and observations (Figs. 11b–c) reveals no demarcation between dry midlevel air and upper-level humidity at  $z_{h^*min}$ . Instead, moist plumes appear to be “pulled” from the boundary layer prior to and during rain events. This is true even for the MMF, which rains very little overall, but mimics the observations during its few rainy periods.

The behavior of CAM precipitation timing and intensity, as well as its midlevel dry bias, can therefore be explained in terms of the formulation of the ZM95 parameterization. In ZM95 the closure is based upon consumption of CAPE. When CAPE is generated, convection must ensue to consume the CAPE. The nature of that convection is determined by  $z_{h^*min}$ . Because  $z_{h^*min}$  is typically found far above the surface, the entrainment rate of the convective plumes in ZM95 must be small enough to allow the plumes to attain that height. This prevents the development of shallow convection, which would rain little but detrain and moisten the lower levels, thereby paving the way for subsequent deeper and, ultimately, more intense convection in the CAM. Dai and Trenberth (2004) also conclude that the early diurnal onset of precipitation in the CAM prevents the buildup of CAPE, which would lead to more intense rainfall.

#### b. Great Plains precipitation in the MMF and CAM

Determining why the MMF produces insufficient rainfall in the Great Plains has been a challenge. Our

FIG. 11. Time–height cross sections of SGP relative humidity (colored contours) for (a) CAM, (b) MMF, and (c) observations. Scaled SGP rainfall is shown in red, and  $z_{h^*min}$  is shown in white. Humidity contours are every 10%. Date range for CAM and MMF is 1 June through 9 September. Date range for observations is 19 June 1997 through 18 July 1997.



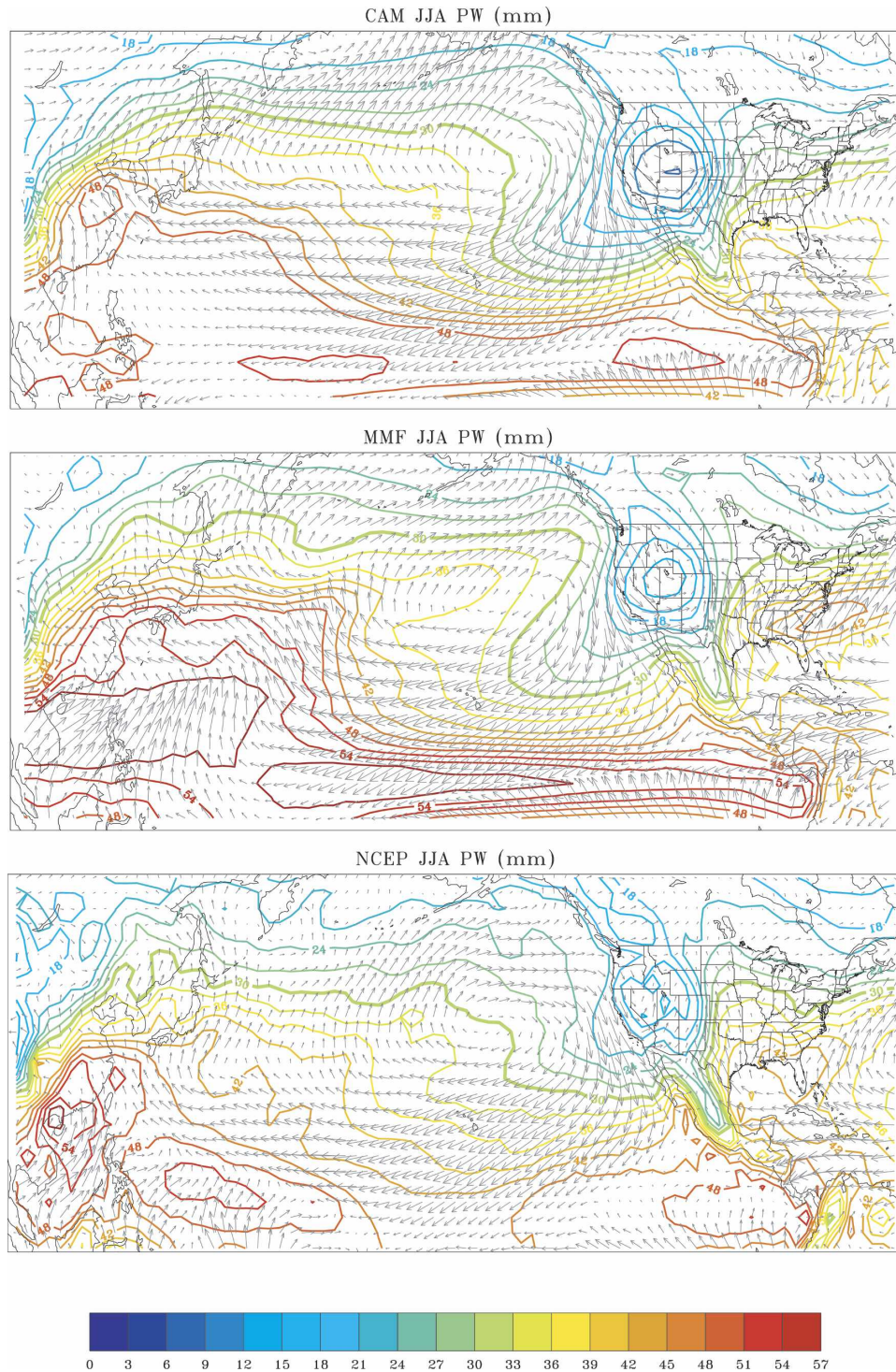


FIG. 12. JJA mean precipitable water content (colored contours) and 900-mb winds (gray arrows) for CAM, MMF, and NCEP reanalysis. The 30-mm contour is thicker than others to facilitate comparison.

initial suspicion was that the MMF had changed the background Great Plains climate so much that we were no longer comparing rainfall production in two similar environments (i.e., between the MMF and CAM). Fig-

ure 12, which shows June–August (JJA) mean precipitable water (PW) content and low-level wind fields, reveals that this is not true. The biggest surprise is that, over the Great Plains (and over the SGP site in Okla-

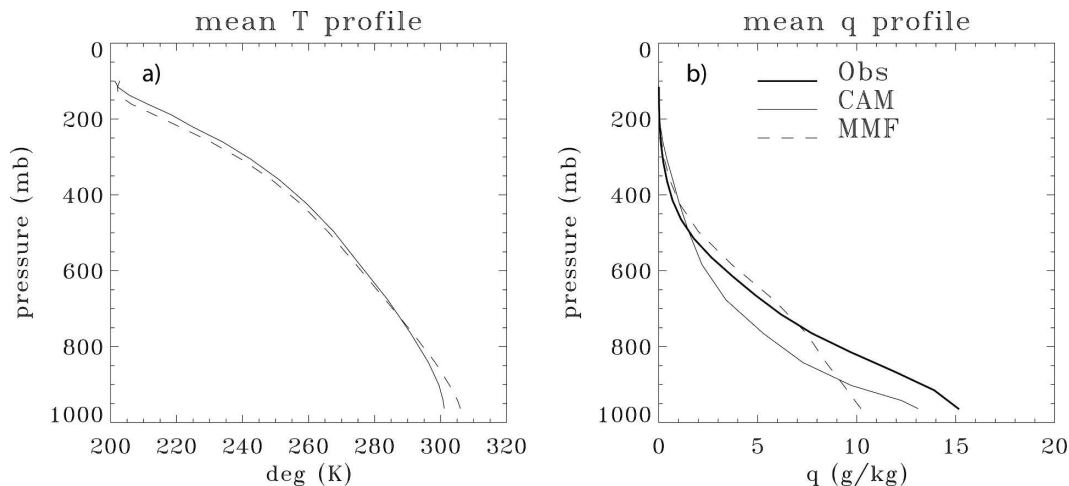


FIG. 13. JJA mean (a) temperature and (b) specific humidity profiles for the SGP grid point for ARM SGP observations and models.

homa in particular), the MMF has a *higher* column water vapor content than the CAM, although both simulations are dry when compared to the observations. Furthermore, both exhibit a realistic low-level jet (LLJ). These findings raise the question of why the CAM produces a realistic seasonal-mean rainfall in the SGP (Fig. 3c), given its simulated dryness relative to the observations.

To address this question, we look at the mean JJA sounding over the North American Great Plains in the two model versions. Figure 13 shows that, compared to the National Centers for Environmental Prediction (NCEP) reanalysis, the CAM is too warm and too dry near the surface, while the MMF agrees well with the reanalysis above  $\sim 700$  mb but is astonishingly warm and dry below this level. How the MMF produces any rain in such an environment is understood by examining the atmospheric state for the five rainiest days for both simulations and the observations. Averaging the soundings for each the five days *before* the five rainiest days (not shown) reveals that both simulations bear a much closer resemblance to the reanalysis than do the respective JJA means. So while the mean environmental state of the MMF is hostile to Great Plains convection, the low levels do occasionally moisten (and cool) to allow convection. Additionally, the correlation between Great Plains rainfall to both surface evaporation and vertically integrated low-level meridional moisture flux (i.e., the low-level jet) are similar for each simulation (not shown), indicating similar moisture sources for rain events in each model version.

The extremely dry lower atmosphere of the MMF in the Great Plains raises the question of whether the land surface is too dry in the MMF. In the following analysis,

we compare the Great Plains with the Amazon Basin since both simulations produce reasonable rainfall totals in the Amazon, but only the CAM produces the right seasonal mean precipitation in the Great Plains. In the ensuing discussion, recall that both simulations use the same surface exchange parameterization, which is applied on the GCM grid. Figure 14 presents time series of monthly mean surface soil moisture content, ground evaporation, canopy evaporation, and canopy transpiration for the Amazon Basin and the Great Plains for both simulations. The sum of the latter three variables is total evaporation into the atmosphere. CAM and MMF have nearly identical near-surface soil moisture contents for both regions (Figs. 14a and 14e), so this cannot explain the dry lower atmosphere in the MMF Great Plains.

In the Amazon Basin, ground evaporation (water evaporated directly from the soil) (Fig. 14b) is nearly identical in DJF for the two simulations. However, canopy evaporation (evaporation of water that rests on the vegetative surface, i.e., from wet leaves) (Fig. 14c) and canopy transpiration (water that is drawn from the soil to the atmosphere via the plants) (Fig. 14d) are distinctly different. In the CAM, canopy evaporation dominates canopy transpiration, while the opposite is true in the MMF. This important difference between the two simulations may be explained by the overall less-intense rainfall found in the CAM. Canopy interception is the process whereby water is intercepted by leaves and prevented from reaching the ground. The efficiency of canopy interception increases for lighter rainfall rates. The low-intensity rain rates in the CAM suggest that an unrealistically large fraction of the rain is intercepted by the canopy and then evaporated from

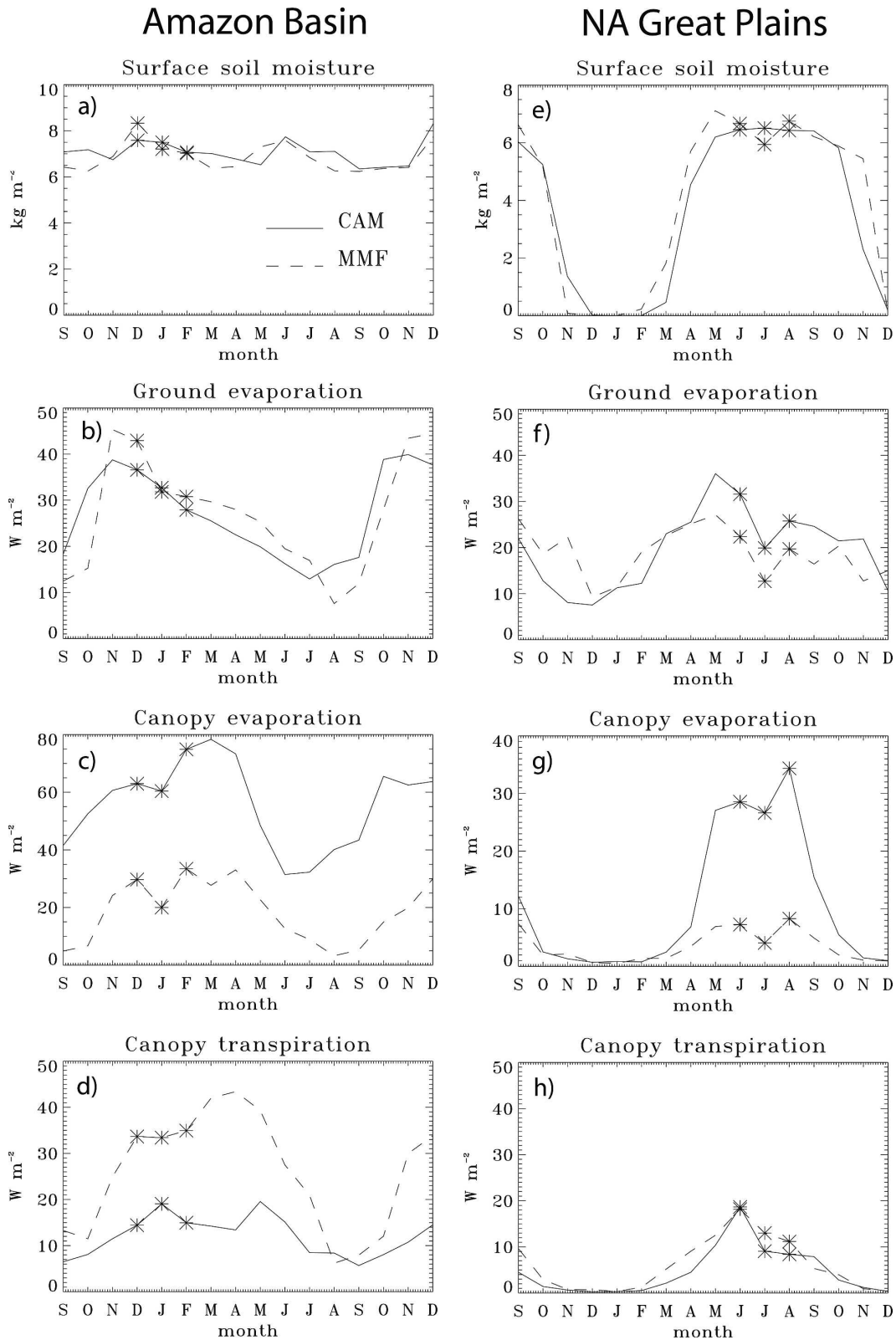


FIG. 14. Time series of monthly mean (a), (e) surface soil moisture, (b), (f) ground evaporation, (c), (g) canopy evaporation, and (d), (h) canopy transpiration for CAM and MMF over the Amazon Basin (DJF: asterisks) and Great Plains (JJA: asterisks).

the leaves, rather than being evaporated or transpired from the ground. In contrast, the heavier rain rates in the MMF put more water directly onto the ground due to lower canopy interception rates. The mean Amazon DJF total surface latent heat fluxes (i.e., the sum of the bottom three panels in Fig. 14) are roughly the same in the two simulations ( $\sim 100 \text{ W m}^{-2}$  for the MMF and  $\sim 115 \text{ W m}^{-2}$  for the CAM), but the water vapor sources are different.

In the Great Plains (Figs. 14e–h), JJA surface soil moisture, ground evaporation, and canopy transpiration are roughly the same for the two simulations, but CAM canopy evaporation exceeds that of the MMF by  $\sim 30 \text{ W m}^{-2}$  during the summer months. Two factors are responsible for this difference. This first is the CAM's larger canopy interception rate, due to its less-intense rain rates, and the second is the tendency of the CAM to produce rainfall nearly every day rather than intermittently, as seen in the MMF and observations (see Fig. 11). Both of these reasons are related to the cumulus entrainment rate selection in ZM95. In fact, it appears that the ZM95 requirement for convection to detrain above  $z_{h^*min}$  may create a positive feedback between light, frequent precipitation and canopy interception. The low simulated rain rates arise from the inability of ZM95 to delay convective development while the boundary layer further energizes. The light rain rates result in increased canopy interception, and the water on the leaves is immediately available for evaporation the following day.

It is interesting to note that the JJA total surface latent heat flux for the CAM is nearly double that of the MMF ( $70 \text{ W m}^{-2}$  versus  $35 \text{ W m}^{-2}$ , respectively). This is the same ratio by which CAM precipitation exceeds MMF precipitation in the Great Plains (Fig. 3c). Since canopy evaporation accounts for nearly half of the total surface latent heat flux in the CAM, we speculate that the recycling of rainwater from the vegetative canopy is artificially increasing the CAM's rainfall totals in this region. Additional analyses of surface exchange data at daily resolution reveal the same behavior in canopy interception (not shown). Furthermore, on days when CAM and MMF daily precipitation are equal, canopy interception is greater in the CAM than in the MMF, which can only occur if CAM *instantaneous* rain rates are less than those produced by the MMF.

## 6. Conclusions

Summertime precipitation variability is used to analyze model performance in two versions of the CAM3, the standard version (CAM) and a modified version

[the multiscale modeling framework (MMF)] in which the cumulus parameterization of Zhang and McFarlane (1995; ZM95) is replaced with the 2D cloud-resolving model of Khairoutdinov and Randall (2003). For three different regions, the CAM produces too narrow a distribution of daily mean rainfall rates, with too much light to moderate rainfall ( $< 10 \sim 20 \text{ mm day}^{-1}$ ). The MMF does a better job of producing the heavier rainfall rates seen in the observations but fails to simulate the lightest rain rates.

We have analyzed high-frequency (3–6 h) covariability between rainfall and atmospheric thermodynamic states for the CAM, the MMF, and the observations. The observations show that, approximately six hours prior to the onset of precipitation, boundary layer moist static energy reaches a maximum, then decreases as increasing convective processes deepen low-level relative humidity. Eventually, the lower atmosphere becomes sufficiently moist to support deep convection, which consumes much of the remaining available boundary layer energy and increases the humidity of the upper troposphere. This series of events is well simulated by the MMF, but in the CAM precipitation, lower- and upper-level humidity, and boundary layer moist static energy all vary in phase with each other. Furthermore, CAM upper- and lower-level relative humidity maxima are separated by a dry midtroposphere. The CAM also exhibits an anomalously strong diurnal cycle of convection compared to the observations.

The formulation of the ZM95 cumulus parameterization offers a physical explanation for many of the CAM's analyzed behaviors. In ZM95 convective closure is based upon consumption of CAPE. When CAPE is present, it must be consumed by convection. ZM95 requires that convective detrainment, which occurs at cloud top, must occur above the level of minimum moist static energy,  $h^*$ . This is arranged by adjusting the convective entrainment rate so that convection reaches this altitude. Comparisons of simulated and observed time series of relative humidity profiles and the height of the minimum of  $h^*$  suggest that this requirement is unrealistic and produces overly deep convection too quickly in the CAM, causing the CAM to rain too soon, too often, and too lightly, thus contributing to its well-documented midlevel dry bias.

Our analysis approach raises the possibility that our conclusions may be unique to the areas we have studied. Sun et al. (2006) employ a convenient way to demonstrate the effects of precipitation intensity on total precipitation by plotting the number of days for which 67% of the annual total rainfall is produced. This is done by sorting daily mean precipitation rates at each grid point from highest to lowest and plotting the num-

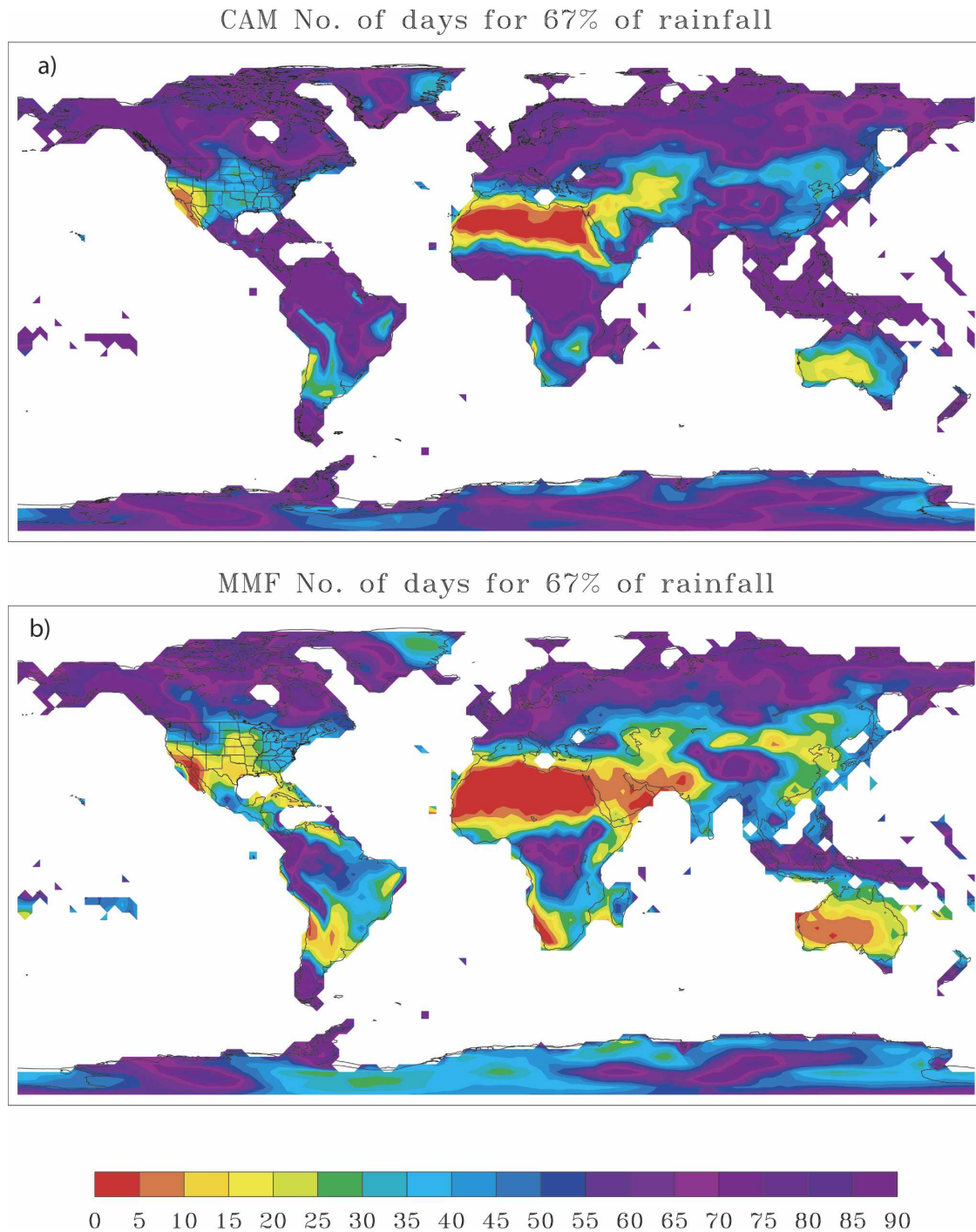


FIG. 15. Map of the number of days needed to reach 67% of annual rainfall for CAM and MMF. See text for details.

ber of days required for 67% of the total. This is shown for the CAM and the MMF in Fig. 15. Figure 1 of Sun et al. (2006) shows that most land-based rainfall is produced over  $\sim 30$  or fewer days. In contrast, the CAM (Fig. 15a) requires 60+ days to attain 67% of total rainfall over most land areas. The MMF (Fig. 15b) re-

quires fewer days needed to reach 67% of the annual mean and agrees well with observations (Fig. 1 of Sun et al. 2006). These results suggest that the conclusions we have drawn, based on detailed analysis at three locations, are representative of simulated precipitation variability worldwide.

Our analysis has identified differences in precipitation variability between the CAM and MMF and has pointed to explanations for some of the differences. Although it was not our intent to demonstrate superiority of one model over another, our analysis has shed light on shortcomings in the CAM. Our analysis did not suggest an explanation for the lack of light rain rates in the MMF. The relatively coarse model resolution of the SAM (4 km) may account for some of the bias but does not appear to be solely responsible.

The MMF has problems in other areas, such as the high rainfall bias in the western Pacific, that were not discussed here due to observational data limitations. Other known issues with the MMF that do not fall into the focus of this study, but need further investigation, are the high zonal wind variability in the Tropics and the overactive Indian monsoon. Future analysis of these topics will help improve our understanding of the underlying physical mechanisms of the real atmosphere as this new modeling approach develops.

*Acknowledgments.* We wish to thank Tom Ackerman, Brian Mapes, Paquita Zuidema, Ed Zipser, Walt Petersen, Sumant Nigam, and Ian Baker for their comments and suggestions. Randy Peppler and Steve Klein provided information on weather patterns of the ARM SGP. NCEP reanalysis data was provided by the NOAA/OAR/ESRL PSD, Boulder, Colorado, from their Web site (<http://www.cdc.noaa.gov/>). This work was supported by ARM Grant DE-FG02-02ER63370, TRMM Grant NAG5-13562, and NOAA Contract NA17RJ1228.

#### REFERENCES

- Arakawa, A., and W. H. Schubert, 1974: Interaction of a cumulus cloud ensemble with the large-scale environment, Part I. *J. Atmos. Sci.*, **31**, 674–701.
- Bonan, G. B., K. W. Oleson, M. Vertenstein, S. Levis, X. Zeng, Y. Dai, R. E. Dickinson, and Z.-L. Yang, 2002: The land surface climatology of the Community Land Model coupled to the NCAR Community Climate Model. *J. Climate*, **15**, 3123–3149.
- Brown, R. A., and J. M. Lewis, 2005: Path to NEXRAD: Doppler radar development at the National Severe Storms Laboratory. *Bull. Amer. Meteor. Soc.*, **86**, 1459–1470.
- Chen, M., R. E. Dickenson, X. Zeng, and A. N. Hahmann, 1996: Comparison of precipitation observed over the continental United States to that simulated by a climate model. *J. Climate*, **9**, 2223–2249.
- Ciesielski, P. E., R. H. Johnson, P. T. Haertel, and J. Wang, 2003: Corrected TOGA COARE sounding humidity data: Impact on diagnosed properties of convection and climate over the warm pool. *J. Climate*, **16**, 2370–2384.
- Collins, W. D., and Coauthors, 2004: Description of the NCAR Community Atmosphere Model (CAM 3.0). Tech. Rep. NCAR/TN-464+STR, National Center for Atmospheric Research, Boulder, CO, 210 pp.
- Dai, A., 2001: Global precipitation and thunderstorm frequencies. Part I: Seasonal and interannual variations. *J. Climate*, **14**, 1092–1111.
- , and K. E. Trenberth, 2004: The diurnal cycle and its depiction in the Community Climate System Model. *J. Climate*, **17**, 930–951.
- , F. Giorgi, and K. E. Trenberth, 1999: Observed and model simulated precipitation diurnal cycles over the contiguous United States. *J. Geophys. Res.*, **104**, 6377–6402.
- Emanuel, K. A., 1994: *Atmospheric Convection*. Oxford University Press, 580 pp.
- Grabowski, W. W., 2001: Coupling cloud processes with the large-scale dynamics using the Cloud-Resolving Convection Parameterization (CRCP). *J. Atmos. Sci.*, **58**, 978–997.
- Groisman, P. Y., R. W. Knight, D. R. Easterling, T. R. Karl, G. C. Hegerl, and V. N. Razuvaev, 2005: Trends in intense precipitation in the climate record. *J. Climate*, **18**, 1326–1350.
- Hack, J. J., B. A. Boville, B. P. Briegleb, J. T. Kiehl, P. J. Rasch, and D. L. Williamson, 1993: Description of the NCAR Community Climate Model (CCM2). Tech. Rep. NCAR/TN-382+STR, National Center for Atmospheric Research, Boulder, CO, 120 pp.
- Haddad, Z. S., E. A. Smith, C. D. Kummerow, T. Iguchi, M. R. Farrar, S. L. Durden, M. Alves, and W. S. Olson, 1997: The TRMM “day-1” radar/radiometer combined rain-profiling algorithm. *J. Meteor. Soc. Japan*, **75**, 799–809.
- Higgins, R. W., J. E. Janowiak, and Y. P. Yao, 1996: *A Gridded Hourly Precipitation Database for the United States (1963–1993)*. NCEP/NCAR Climate Prediction Center Atlas No. 1, U.S. Dept. of Commerce, 47 pp.
- Huffman, G. J., R. F. Adler, M. Morrissey, D. T. Bolvin, S. Curtis, R. Joyce, B. McGavock, and J. Susskind, 2001: Global precipitation at one-degree daily resolution from multisatellite observations. *J. Hydrometeorol.*, **2**, 36–50.
- Iorio, J., P. B. Duffy, B. Govindasamy, S. L. Thompson, M. Khairoutdinov, and D. A. Randall, 2004: Effects of model resolution and subgrid-scale physics on the simulation of precipitation in the continental United States. *Climate Dyn.*, **23**, 243–258.
- Johnson, R. H., and P. E. Ciesielski, 2000: Rainfall and radiative heating rate estimates from TOGA COARE atmospheric budgets. *J. Atmos. Sci.*, **57**, 1497–1514.
- Karl, T. R., and R. W. Knight, 1998: Secular trends of precipitation amount, frequency, and intensity in the United States. *Bull. Amer. Meteor. Soc.*, **79**, 231–241.
- Khairoutdinov, M. F., and D. A. Randall, 2001: A cloud resolving model as a cloud parameterization in the NCAR Community Climate System Model: Preliminary results. *Geophys. Res. Lett.*, **28**, 3617–3620.
- , and —, 2003: Cloud resolving modeling of the ARM Summer 1997 IOP: Model formulation, results, uncertainties, and sensitivities. *J. Atmos. Sci.*, **60**, 607–625.
- , —, and C. DeMott, 2005: Simulations of the atmospheric general circulation using a cloud-resolving model as a superparameterization of physical processes. *J. Atmos. Sci.*, **62**, 2136–2154.
- Khari, V. V., F. W. Zwiers, and X. Zhang, 2005: Intercomparison of near-surface temperature precipitation extremes in AMIP-2 simulations, reanalyses, and observations. *J. Climate*, **18**, 5201–5223.
- Leone, D. A., R. M. Endlich, J. Petrieks, R. T. H. Collis, and J. R.

- Porter, 1989: Meteorological considerations used in planning the NEXRAD Network. *Bull. Amer. Meteor. Soc.*, **70**, 4–13.
- Liebmann, B., G. N. Kiladis, J. A. Marengo, T. Ambrizzi, and J. D. Glick, 1999: Submonthly convective variability over South America and the South Atlantic convergence zone. *J. Climate*, **12**, 1877–1891.
- Oleson, K. W., G. B. Bonan, S. Levis, and M. Vertenstein, 2004: Effects of land use change on North American climate: Impact of surface datasets and model biogeophysics. *Climate Dyn.*, **23**, 117–132.
- Petersen, W. A., S. A. Nesbitt, R. J. Blakeslee, R. Cifelli, P. Hein, and S. A. Rutledge, 2002: TRMM observations of intraseasonal variability in convective regimes over the Amazon. *J. Climate*, **15**, 1278–1294.
- Reynolds, R. W., N. A. Rayner, R. M. Smith, D. C. Stokes, and W. Wang, 2002: An improved in situ and satellite SST analysis for climate. *J. Climate*, **15**, 1609–1625.
- Roy, B., and J. B. Halverson, 2002: On quality control procedures being adopted for TRMM LBA and KWAJEX soundings data sets. Preprints, *Symp. on Observations, Data Assimilation, and Probabilistic Prediction*, Orlando, FL, Amer. Meteor. Soc., CD-ROM, P2.6.
- Silva Dias, M. A. F., and Coauthors, 2002: Clouds and rain processes in a biosphere-atmosphere interaction context in the Amazon region. *J. Geophys. Res.*, **107**, 8072, doi:10.1029/2001JD000335.
- Sobel, A. H., S. E. Yuter, C. S. Bertherton, and G. N. Kiladis, 2004: Large-scale meteorology and deep convection during TRMM KWAJEX. *Mon. Wea. Rev.*, **132**, 422–444.
- Sun, Y., S. Solomon, A. Dai, and R. W. Portmann, 2006: How often does it rain? *J. Climate*, **19**, 916–934.
- Trenberth, K. E., A. Dai, R. M. Rasmussen, and D. B. Parsons, 2003: The changing character of precipitation. *Bull. Amer. Meteor. Soc.*, **84**, 1205–1217.
- Webster, P. J., and R. Lukas, 1992: TOGA COARE: The coupled ocean-atmosphere response experiment. *Bull. Amer. Meteor. Soc.*, **73**, 1377–1416.
- Wilcox, E. M., and L. J. Donner, 2007: The frequency of extreme rain events in satellite rain-rate estimates and an atmospheric general circulation model. *J. Climate*, **20**, 53–69.
- Zhang, G. J., and N. A. McFarlane, 1995: Sensitivity of climate simulations to the parameterization of cumulus convection in the Canadian Climate Centre general circulation model. *Atmos.–Ocean*, **33**, 407–446.
- , J. T. Kiehl, and P. J. Rasch, 1998: Response of climate simulation to a new convective parameterization in the National Center for Atmospheric Research Community Climate Model (CCM3). *J. Climate*, **11**, 2097–2115.
- Zhang, M. H., and J. L. Lin, 1997: Constrained variational analysis of sounding data based on column-integrated conservations of mass, heat, moisture, and momentum: Approach and application to ARM measurements. *J. Atmos. Sci.*, **54**, 1503–1524.
- , —, R. T. Cederwall, J. J. Yio, and S. C. Xie, 2001: Objective analysis of ARM IOP data: Method and sensitivity. *Mon. Wea. Rev.*, **129**, 295–311.